



# Enhanced photoelectrochemical performance of planar p-Silicon by APCVD deposition of surface mesoporous hematite coating



Shipu Li<sup>a</sup>, Peng Zhang<sup>a,\*</sup>, Xiaofeng Xie<sup>b</sup>, Xuefeng Song<sup>a</sup>, Jing Liu<sup>a</sup>, Liping Zhao<sup>a</sup>, Han Chen<sup>a</sup>, Lian Gao<sup>a,\*</sup>

<sup>a</sup> State Key Lab of Metal Matrix Composites, School of Materials Science and Engineering, Shanghai Jiao Tong University, Shanghai, 200240, China

<sup>b</sup> State Key Laboratory of High Performance Ceramics and Superfine Microstructure, Shanghai Institute of Ceramics, Chinese Academy of Sciences, Shanghai, 200050, China

## ARTICLE INFO

### Article history:

Received 23 February 2016

Received in revised form 2 July 2016

Accepted 19 July 2016

Available online 19 July 2016

## ABSTRACT

Pt nanoparticles are the most frequently used catalyst for Si photocathode. Alternative catalyst based on transition metal or metal oxide as cathode catalyst is greatly desired to replace Pt. A mesoporous  $\alpha$ -Fe<sub>2</sub>O<sub>3</sub> thin film (80 nm) was deposited on the surface of planar p-Si using a facile atmospheric pressure chemical vapor deposition (APCVD) method through pyrolysis of ferrocene. The planar Si photocathode shows a 400% enhancement in photocurrent at  $-1.0\text{ V}_{\text{RHE}}$  and an anodic onset potential shift of 0.5 V upon deposition of surface mesoporous  $\alpha$ -Fe<sub>2</sub>O<sub>3</sub> layer. This composite photoelectrode also shows superior photoelectrochemical performance to the Pt/planar Si photoelectrode.

© 2016 Elsevier B.V. All rights reserved.

### Keywords:

Planar Si  
 $\alpha$ -Fe<sub>2</sub>O<sub>3</sub>  
 Catalysts  
 Photoelectrochemistry  
 Hydrogen

## 1. Introduction

Hydrogen is one of a candidate answer to the energy and environmental puzzle of the current society due to its zero CO<sub>2</sub> emission. The demand of hydrogen will face a significant increase upon the large scale use of hydrogen fuel cell vehicles in future. However, the current industrial production of hydrogen is mainly from fossil fuel reforming or coal gasification, which still produce CO<sub>2</sub> emission during production. The totally clean manufacture of hydrogen is by electrolysis of water driven by solar energy. Photoelectrochemical (PEC) water splitting is a promising and environmentally benign method for solar hydrogen generation, which has cost advantage over the direct electrolysis on electrolytic equipment using photovoltaic devices [1–10]. A variety of photoelectrodes have shown high efficiency in hydrogen production using solar energy, such as Cu<sub>2</sub>O, Cu<sub>2</sub>ZnSnS<sub>4</sub>, InP, InGaN, etc [11–14]. Silicon is the second most abundant element in the earth's crust with a narrow band gap ( $E_g = 1.1\text{ eV}$ ), which is widely applied in photovoltaic industry and proved to be efficient as photoelectrodes for solar hydrogen production [14–17].

In order to lower the external bias that is required to drive water splitting reaction, a variety of precious metal catalysts have been used to reduce the onset potential [18–20]. Transition metal oxides, such as NiO<sub>x</sub>, NiRuO<sub>x</sub> and Fe<sub>2</sub>O<sub>3</sub>, have also shown promising potential as catalyst for surface oxygen evolution on Si photoanodes [21–23]. Recently, researchers have paid much attention to the application of metal oxides to enhance the PEC performance of photocathode. Hematite ( $\alpha$ -Fe<sub>2</sub>O<sub>3</sub>) as a photoanode material has received considerable attention due to its abundance, low cost, excellent chemical stability, and favorable band gap energy of  $1.9 \sim 2.2\text{ eV}$ , sufficient to utilize approximately 40% of the incident sunlight. A big variety of synthesis methods, e.g. hydrothermal [24], sol-gel [25,26], electrodeposition [27,28], anodization [29], spray pyrolysis [30], atomic layer deposition (ALD) [31] and atmospheric pressure chemical vapor deposition (APCVD) [3], have been developed to construct hematite thin films as photoanodes. In our previous work [2], we reported a facile method for deposition of ultrathin  $\alpha$ -Fe<sub>2</sub>O<sub>3</sub> thin film using ferrocene as iron oxide precursors. However, hematite has been rarely reported as efficient catalyst for PEC H<sub>2</sub> production.

Herein, the facile APCVD method using ferrocene precursor is utilized to deposit hematite thin films on the surface of planar p-Si for preparation of  $\alpha$ -Fe<sub>2</sub>O<sub>3</sub>/Si composite photoelectrode. The as-deposited hematite coating layer well catalysed the PEC H<sub>2</sub> pro-

\* Corresponding authors.

E-mail addresses: pengzhang2010@sjtu.edu.cn (P. Zhang), liangao@mail.sic.ac.cn (L. Gao).

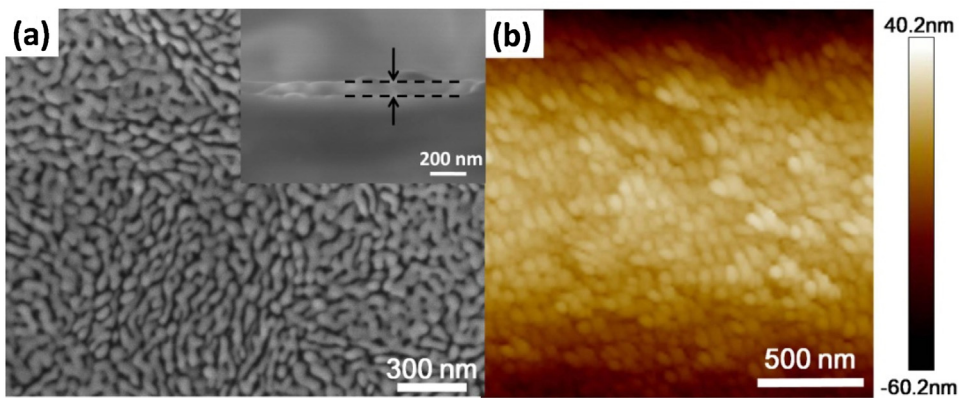


**Fig. 1.** (a) Top and cross-section (inset) SEM images, and (b) AFM image of  $\alpha\text{-Fe}_2\text{O}_3/\text{Si}$  photoelectrode.

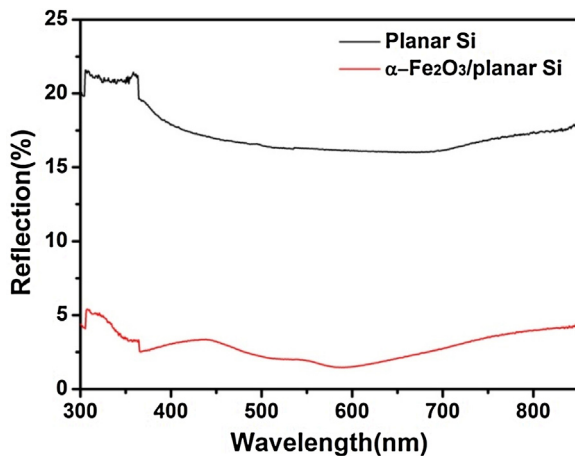


**Fig. 2.** UV-vis reflection spectra of planar Si and  $\alpha\text{-Fe}_2\text{O}_3/\text{Si}$  photoelectrode.

duction of the planar p-Si in both alkaline and neutral solutions, the efficiency of which even overwhelmed the Pt/Si nanowires.

## 2. Experimental

### 2.1. Preparation of $\alpha\text{-Fe}_2\text{O}_3/\text{Si}$ photoelectrode

In this work, boron doped P-type silicon wafers (with resistivity of 0.01–1  $\Omega\text{cm}$ ) with crystal orientation of (100) were used. Firstly, the wafer was cut into small chips ( $1 \times 2 \text{ cm}$ ). All the chips were degreased by sonication in acetone, ethanol, deionized water, respectively. Then the samples were thoroughly rinsed with deionized water and dipped into a solution of HF to remove the  $\text{SiO}_2$  layer on the Si chip surface. The Si chip was fixed on the top of a crucible (50 ml) loaded with 0.1 g ferrocene. The setup was covered with quartz glass and annealed at 550 °C for 2 h. On the back side of the Si chip, an ohmic contact was established by embedding a Cu wire in a eutectic gallium-indium alloy. The Cu wire and the eutectic alloy were subsequently covered with silver paint. The epoxy was further used to insulate the entire back side of the electrode and the Cu wire from the electrolyte. The exposed area on the front side of the Si electrode is 1  $\text{cm}^2$ .

### 2.2. Characterization

The morphologies and surface roughness of the as-prepared samples were observed using a field-emission scanning electron microscope (FESEM, FEI, Sirion 200) and Atomic Force Microscopy (AFM) on a MultiMode 8 (Bruker) in scanasyst mode. Energy dis-

persive X-ray (EDX) spectrum, and the corresponding elemental mapping of the samples were obtained on a FESEM equipped with an EDX spectrometer. The absorption properties of the samples were recorded using a reflectance UV-vis spectrometer (UV-3600, SHIMADZU). X-ray photoelectron spectroscopic (XPS) measurements were performed on a Kratos AXIS Ultra DLD spectrometer. The crystallographic structures of the as-synthesized products were identified by X-ray diffraction (XRD, Ultima IV, Rigaku Co., LTD, Japan Cu K $\alpha$ ,  $\lambda = 1.54178 \text{ \AA}$ ). The crystalline phase was confirmed by Raman spectrometer (LabRAM HR Evolution).

### 2.3. Photoelectrochemical measurements

All PEC measurements were carried out using CHI 660D electrochemical workstation in a standard three electrode configuration with a platinum wire as the counter electrode, a saturated calomel electrode (SCE) as the reference electrode, and the as-prepared samples as the working electrode. 1 M NaOH and 1 M Na<sub>2</sub>SO<sub>4</sub> were used as the electrolytes. The simulated illumination of 1 sun was provided by 300 W Xenon lamp with AM 1.5 filter. The IPCE (incident photon-to-current conversion efficiency) of the photoelectrode was measured under monochromatic illumination provided by SM-250 Hyper Monolight System (Bunkoukeiki, Japan).

## 3. Results and discussion

### 3.1. Morphology

**Fig. 1** shows the SEM and AFM images of  $\alpha\text{-Fe}_2\text{O}_3/\text{Si}$  photoelectrode. The surface morphology of  $\alpha\text{-Fe}_2\text{O}_3/\text{Si}$  photoelectrode thin film shows mesoporous structure composed of rod shaped nanoparticles. The cross-section image shows a thickness of ~80 nm. This is similar to the  $\alpha\text{-Fe}_2\text{O}_3$  thin film grown on the Ti foil, which consists a monolayer of 50 nm nanoparticles [2]. The ultrathin structure of hematite could overcome, in some degree, its intrinsic poor conductivity [32,33]. The mesoporous Fe<sub>2</sub>O<sub>3</sub> layer allows the direct contact of the underneath Si surface with the electrolyte. The AFM image of  $\alpha\text{-Fe}_2\text{O}_3/\text{Si}$  photoelectrode shows consistent morphology with the SEM image, and a much higher surface roughness than the planar Si [34]. The measured surface root-mean-square roughness ( $R_q$ ) of  $\alpha\text{-Fe}_2\text{O}_3/\text{Si}$  photoelectrode is 17.2 nm, much larger than 0.567 nm of planar Si. The rough mesoporous surface structure made of hematite nanoparticles shall facilitate the desorption of H<sub>2</sub> bubbles from the electrode surface, which avoids the obstruction of electrolyte by big gas bubbles on the surface and the resultant kinetic limitation in surface reduction reaction during the PEC hydrogen production. The EDX-mapping

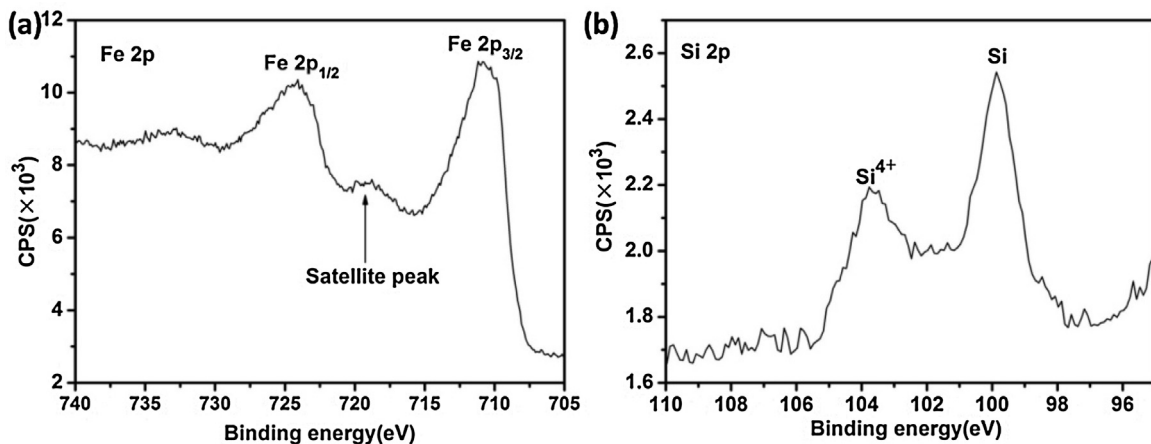


**Fig. 3.** The X-ray photoelectron spectrum of (a) Fe 2p and (b) Si 2p collected from  $\alpha\text{-Fe}_2\text{O}_3/\text{Si}$  photoelectrode.

images (Fig. S1) show obvious presence of both Fe and Si, which confirms the presence of surface mesoporous structure.

### 3.2. UV-vis reflection spectra

The untreated planar silicon wafer has a mirror-like surface, which has a poor capability for light capture. The surface becomes dark blue after  $\alpha\text{-Fe}_2\text{O}_3$  coating. This difference in optical absorption is confirmed by their UV-vis diffuse reflection spectra, Fig. 2. The reflectance of  $\alpha\text{-Fe}_2\text{O}_3/\text{Si}$  sample is drastically reduced comparing to the planar Si. The superior antireflection properties of the  $\alpha\text{-Fe}_2\text{O}_3/\text{Si}$  can be attributed to its higher surface roughness. Therefore, the darkness of the surface of planar silicon induced by deposition of hematite nanoparticles is similar to the silicon nanowires grown through surface etching of the planar Si. From the reflection spectra, we can also find that both samples show broad absorption in the visible light.

### 3.3. XPS analysis

The elemental composition of the  $\alpha\text{-Fe}_2\text{O}_3/\text{Si}$  photoelectrode was determined by XPS. The XPS shows binding energy of Fe  $2p_{1/2}$  and Fe  $2p_{3/2}$  of the composite photoelectrode at 724.2 eV and 711 eV, respectively, in Fig. 3(a). The satellite peak at 719.6 eV is characteristic of  $\alpha\text{-Fe}_2\text{O}_3$  [35]. These indicate that  $\alpha\text{-Fe}_2\text{O}_3$  thin film was obtained on the surface of planar Si through pyrolysis of ferrocene in the air at 550 °C. The  $\alpha\text{-Fe}_2\text{O}_3$  crystalline phase was further confirmed by the XRD and Raman spectrum, Fig. S2. The spectrum of the Si 2p region of  $\alpha\text{-Fe}_2\text{O}_3/\text{Si}$  photoelectrode, Fig. 3(b), indicates the presence of  $\text{SiO}_2$  due to the binding energy at 103.5 eV. These two obvious peaks prove that there is a  $\text{SiO}_2$  layer between the  $\alpha\text{-Fe}_2\text{O}_3$  layer and the Si substrate. The  $\text{SiO}_2$  layer might come from the oxidized surface of silicon during deposition of hematite surface layer that was carried out in the air at 550 °C.

### 3.4. PEC performance

The chopped I-V curves of planar Si, Pt/planar Si and  $\alpha\text{-Fe}_2\text{O}_3/\text{Si}$  photoelectrode under AM 1.5 G illumination are presented in Fig. 4(a) for comparison. All samples show photocathodic performances. The  $\alpha\text{-Fe}_2\text{O}_3/\text{Si}$  shows advantage over both planar Si and Pt/planar Si in both photocurrents and onset potentials. At an applied bias of  $-1.5 \text{ V}_{\text{RHE}}$ , the photocurrent of the  $\alpha\text{-Fe}_2\text{O}_3/\text{Si}$  photoelectrode reaches  $-34 \text{ mA/cm}^2$ , which is much higher than  $-20 \text{ mA/cm}^2$  of the planar Si,  $-27 \text{ mA/cm}^2$  of Pt/planar Si, and the reported Si nanowires with surface Pt nanoparticles

( $\sim -27 \text{ mA/cm}^2$ ) [20]. This photocurrent is also among the highest ever reported for p-Si based photoelectrodes. At applied bias of  $-0.6 \text{ V}_{\text{RHE}}$ , the photocurrent of the as prepared  $\alpha\text{-Fe}_2\text{O}_3/\text{Si}$  photoelectrode is  $-30 \text{ mA/cm}^2$ , which is also much higher than  $-2 \text{ mA/cm}^2$  for the planar Si photoelectrode and the  $-23 \text{ mA/cm}^2$  for Pt/planar Si. The onset potential of  $\alpha\text{-Fe}_2\text{O}_3/\text{Si}$  photoelectrode is anodically shifted by 0.5 V relative to the bare planar Si. The onset potential of mesoporous  $\alpha\text{-Fe}_2\text{O}_3/\text{Si}$ , 0.25  $\text{V}_{\text{RHE}}$ , is also less negative than the Pt/planar Si, Fig. 4a, as well as in the previous report [34]. It is obvious that the surface hematite layer increase the photocurrent and shift onset potential anodically. Therefore, hematite surface layer plays the role of surface catalyst as the Pt nanoparticles in the case of Pt/planar Si. The improved optical absorption and the probable junction between p-Si and  $\alpha\text{-Fe}_2\text{O}_3$ , which facilitates the separation of photo-generated electron-hole pairs, might also contribute to the enhanced PEC performance. This result is also consistent with the  $\alpha\text{-Fe}_2\text{O}_3/\text{SnO}_2/\text{Si}$  NW reported by Kargar [36]. They proposed that the improved photocathodic performance can be indexed to the nano-textured shell, which has a higher surface area and better optical absorption. Contributions to the high measured current from other probable alternate sources including etching of silicon and iron oxide were also ruled out by explicit consideration of the overall volume of the involved semiconductor and any resultant valence charge contribution [21].

The enhanced solid-liquid interface area of the  $\alpha\text{-Fe}_2\text{O}_3/\text{Si}$  photoelectrode relative to the planar Si is illustrated by the increased capacitance of the double layers (Fig. S3) that is related to the electrochemical active surface areas. A higher contact area is beneficial to the electrolyte diffusion onto the surface of the electrode and to the increased PEC performance [10]. When organic reactant is added in the electrolyte, the photocurrent can be further increased, Fig. S4. The advantageous oxidation kinetics of methanol molecules relative to water molecules on the counter electrode boosts the PEC redox reaction. This also demonstrates the ability of the photoelectrodes in degradation of organic chemicals during the production of hydrogen using solar energy.

The IPCE of  $\alpha\text{-Fe}_2\text{O}_3/\text{Si}$  photoelectrode in Fig. 4(b) shows PEC response over a wide spectral range corresponding to the silicon band gap energy of 1.12 eV ( $\lambda=1109 \text{ nm}$ ), which is consistent to the reflection spectra in Fig. 2. The value of IPCE increases rapidly with wavelength decreasing from 1000 nm, and reaches the maximum of 70% at 600 nm. This maximum at 600 nm could be partially related to the absorption of hematite below 600 nm, which however has no contribution to the photocurrents due to the poor PEC performance of the undoped hematite photoanode prepared at low temperature. The hematite anode generally show maximum IPCE

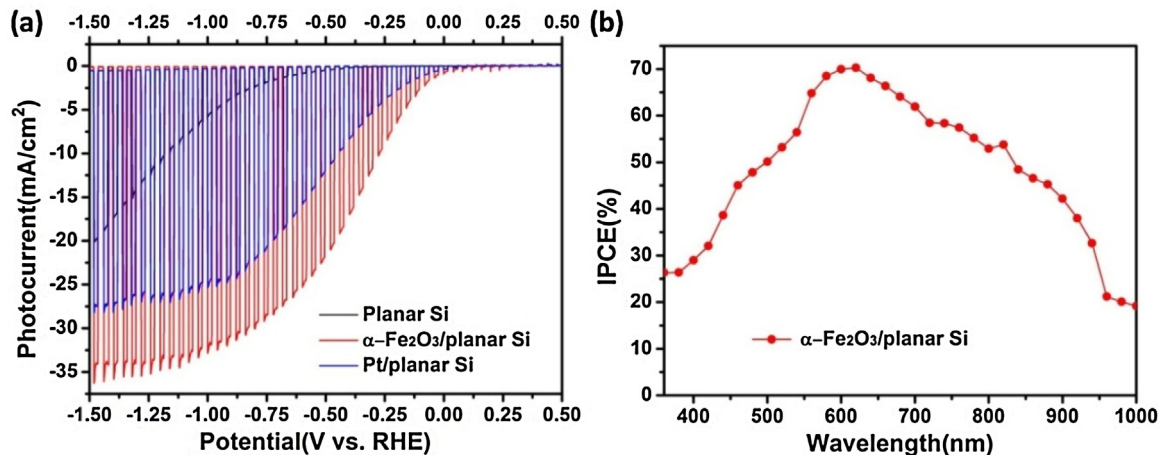


**Fig. 4.** (a) Chopped I-V curves of planar Si, Pt/planar Si and  $\alpha$ -Fe<sub>2</sub>O<sub>3</sub>/Si photoelectrode and (b) IPCE performance of  $\alpha$ -Fe<sub>2</sub>O<sub>3</sub>/Si photoelectrode at  $-1$  V<sub>RHE</sub> measured in 1 M NaOH solution.

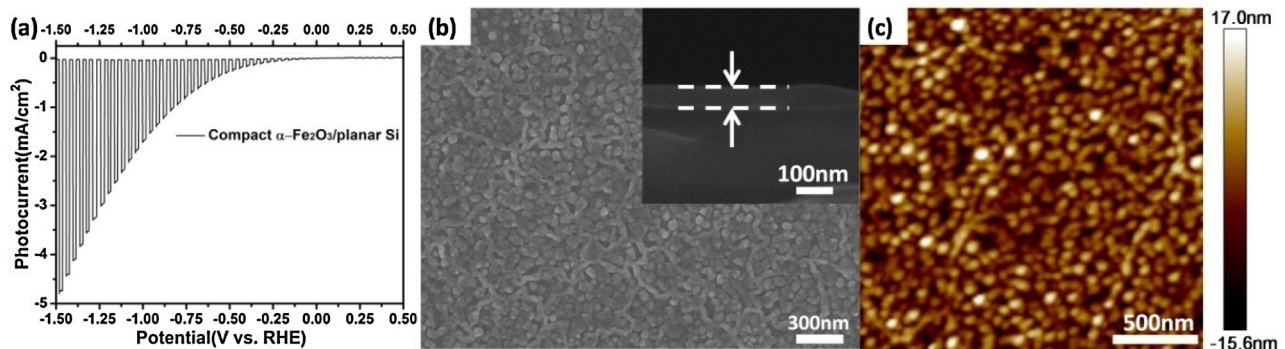


**Fig. 5.** (a) Chopped I-V curve, (b) SEM image and (c) AFM image of compact  $\alpha$ -Fe<sub>2</sub>O<sub>3</sub>/Si photoelectrode, prepared by sputtering of Fe metal on planar silicon wafer followed by oxidation at 550 °C for 2 h.

at  $\sim 400$  nm and almost zero at 600 nm [3]. These observations suggest that the photocurrent arises from Si rather than  $\alpha$ -Fe<sub>2</sub>O<sub>3</sub> layer [21].

The effect of the surface morphology of the Fe<sub>2</sub>O<sub>3</sub> was investigated on the PEC performance of the composite photoelectrode. A compact Fe<sub>2</sub>O<sub>3</sub> layer was deposited by sputtering Fe metal on planar Si followed by oxidation in the air at 550 °C for 2 h. The as deposited Fe<sub>2</sub>O<sub>3</sub>, Fig. 5, shows a relatively smoother surface than APCVD method and a similar thickness of 80 nm. Its surface root-mean-square roughness ( $R_q$ ) is 4.6 nm, which is much lower than the 17.2 nm of the mesoporous  $\alpha$ -Fe<sub>2</sub>O<sub>3</sub>/Si photoelectrode. The onset potential of this sample is 300 mV negative relative to the mesoporous Fe<sub>2</sub>O<sub>3</sub>/Si. The photocurrent is also significantly reduced with the compact Fe<sub>2</sub>O<sub>3</sub> layer, which is  $-4.7$  mA/cm<sup>2</sup> at  $-1.5$  V<sub>RHE</sub> (Fig. 5a). In contrast, the mesoporous structure showed significant advantage, Fig. 1(a). Kargar suspected the increased photocurrent and anodically shifted onset potential in both neutral and basic solution can be attributed to the enhancement in the surface roughness [36]. Therefore, the mesoporous surface feature of hematite deposited by ferrocene oxidation is favored for hydrogen evolution rather than the compact hematite thin films coated on the surface of planar silicon. This indicates that the H<sub>2</sub> bubbles from the interface between Fe<sub>2</sub>O<sub>3</sub> and Si, where Fe<sub>2</sub>O<sub>3</sub> works as catalyst for proton reduction and the mesopores of the top layer facilitates the evolution of H<sub>2</sub> from the surface of the bottom Si layer. The compact hematite top layer, however, has very limited

space for the evolution of the as-produced H<sub>2</sub> from the bottom Si layer. We propose that the H<sub>2</sub> evolves from the Fe<sub>2</sub>O<sub>3</sub>-Si interface instead of Fe<sub>2</sub>O<sub>3</sub> surface because the 80 nm of hematite is too thick for photo-generated electrons to tunnel through or transport due to the poor conductivity of hematite [37]. This is consistent with the reported Fe<sub>2</sub>O<sub>3</sub> surface layers as catalysts for either photocathode or photoanode, which all have a small surface feature and a mesoporous structure facilitating the evolution of gases [21,36].

It was reported that the deposition of Fe<sub>2</sub>O<sub>3</sub> of  $\sim 20$  nm on the n-Si significantly improve the O<sub>2</sub> evolution reaction and the resulted anodic photocurrent [21]. The improvement of the photocurrent was proved to be the catalytic effect of Fe<sub>2</sub>O<sub>3</sub> instead of etching of Si in the strong basic electrolyte (pH = 13.8). Herein, the 80 nm mesoporous Fe<sub>2</sub>O<sub>3</sub> thin film well catalyze the photocathodic H<sub>2</sub> evolution reaction on p-Si photocathode. From Fig. 4, the catalytic effect is even better than Pt nanoparticles. The band edge alignment of Fe<sub>2</sub>O<sub>3</sub> and Si might also contribute to this effect [36]. The photocurrent at 0 V<sub>RHE</sub> in 1 M NaOH is  $\sim -0.75$  mA/cm<sup>2</sup>, Fig. 6(a), which is higher than  $-0.08$  mA/cm<sup>2</sup> of the Si/SnO<sub>2</sub>/Fe<sub>2</sub>O<sub>3</sub> under the same condition [36]. This photocurrent can be further increased to  $-1.6$  mA/cm<sup>2</sup> with the presence of methanol, as shown in the continuous test in Fig. S5. The photocurrent in neutral Na<sub>2</sub>SO<sub>4</sub> solution is  $\sim -0.1$  mA/cm<sup>2</sup>, Fig. 6(b), which is also higher than Si/SnO<sub>2</sub>/Fe<sub>2</sub>O<sub>3</sub> photoelectrode. Considering the facile deposition method of mesoporous Fe<sub>2</sub>O<sub>3</sub> in our case, the composite photoelectrode Fe<sub>2</sub>O<sub>3</sub>/Si

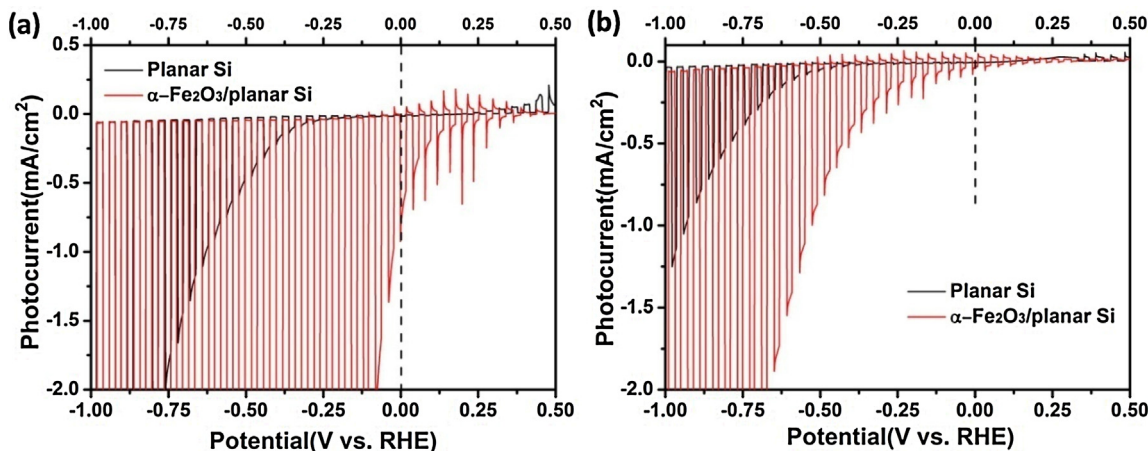


**Fig. 6.** The photocurrent of the planar Si and  $\alpha$ -Fe<sub>2</sub>O<sub>3</sub>/Si photoelectrode at 0 V<sub>RHE</sub> measured in (a) 1 M NaOH and (b) 1 M Na<sub>2</sub>SO<sub>4</sub>.

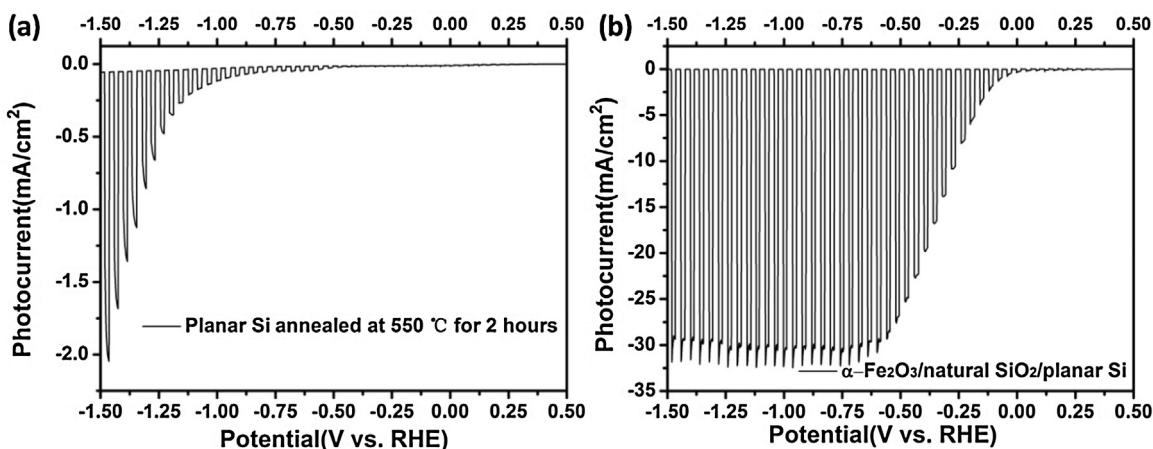


**Fig. 7.** (a) Chopped I-V curves of the planar Si photoelectrode annealed at 550 °C for 2 h and  $\alpha$ -Fe<sub>2</sub>O<sub>3</sub>/natural SiO<sub>2</sub>/Si photoelectrode.

prepared by APCVD method shows advantages in both the preparation and PEC performance.

According to the preparation procedure and the XPS results, there is SiO<sub>2</sub> layer under the Fe<sub>2</sub>O<sub>3</sub> thin film, which might separates the direct contact between Si metal and Fe<sub>2</sub>O<sub>3</sub> catalyst. When the planar Si wafer was annealed at 550 °C for 2 h in air and prepared as photoelectrode using the same procedure, the photoresponse is very poor (Fig. 7a). The direct deposition of hematite on untreated silicon wafer, which has natural SiO<sub>2</sub> surface layer, leads to a photoresponse close to the sample in Fig. 4 (Fig. 7b). Therefore, the hematite nanoparticles on the surface of silicon wafer behaves as surface catalyst for surface hydrogen production upon reduction of proton by electrons. The thickness of SiO<sub>2</sub> layer between hematite catalyst and silicon metal plays an important role in the performance due to the difficulties in tunneling the SiO<sub>2</sub> layer for electrons.

Hematite nanoparticles well catalyze the surface hydrogen evolution reaction of the silicon photocathodes. However, the durability of the surface hematite coating layer on the planar substrate needs to be further improved. Under 100 mW/cm<sup>2</sup> illumination, the composite photoelectrode shows degradation (~6%) in photocurrent density after 100 min, Fig. S6. The SEM images of the photoelectrode, Fig. S7, illustrate partial peeling off of the surface hematite particles after long term reaction, which explains the degraded photocurrents. The interaction between the hematite particles deposited by the pyrolysis and the substrate might be not strong enough to sustain the continuous intensive H<sub>2</sub> bubbling

from the grain boundaries. Upon the addressing of the strategies to improve the durability of the Fe<sub>2</sub>O<sub>3</sub>/Si composite structures, the advantages of hematite as hydrogen evolution catalyst will be fully exploited.

#### 4. Conclusion

In summary, the  $\alpha$ -Fe<sub>2</sub>O<sub>3</sub>/Si photoelectrode produces a much higher photocurrent than the planar Si photoelectrode and Pt/planar Si photoelectrode. The cathodic photocurrent of the  $\alpha$ -Fe<sub>2</sub>O<sub>3</sub>/Si photoelectrode reaches ~34 mA/cm<sup>2</sup> under 100 mW/cm<sup>2</sup> illumination at -1.5 V<sub>RHE</sub>. The onset potential of  $\alpha$ -Fe<sub>2</sub>O<sub>3</sub>/Si photoelectrode is anodically shifted by 0.5 V relative to the bare planar Si. The maximum IPCE of  $\alpha$ -Fe<sub>2</sub>O<sub>3</sub>/Si photoelectrode is 70% at 600 nm. The photoelectrochemical hydrogen production was proposed to be catalysed by surface hematite nanoparticles on the interface of hematite and silicon.

#### Acknowledgments

The authors greatly acknowledge the financial support by the National Natural Science Foundation of China (No.51172142, 51302169), Shanghai Municipal Natural Science Foundation (No.12ZR1414300), and the Third Phase of 211 Project for Advanced Materials Science (No.WS3116205007). This research is also supported by the Opening Project of State Key Labora-

tory of High Performance Ceramics and Superfine Microstructure (SKL201305SIC).

## Appendix A. Supplementary data

Supplementary data associated with this article can be found, in the online version, at <http://dx.doi.org/10.1016/j.apcatb.2016.07.031>.

## References

- [1] A. Fujishima, K. Honda, *Nature* 238 (1972) 37–38.
- [2] P. S. Li, X. Zhang, L. Song, *Int. J. Hydrogen Energy* 39 (2014) 14596–14603.
- [3] P. Zhang, A. Kleiman-Shwarsztejn, Y.S. Hu, J. Lefton, S. Sharma, A.J. Forman, E. McFarland, *Energy Environ. Sci.* 4 (2011) 1020–1028.
- [4] X. Wang, K.Q. Peng, Y. Hu, F.Q. Zhang, B. Hu, L. Li, M. Wang, X.M. Meng, S.T. Lee, *Nano Lett.* 14 (2014) 18–23.
- [5] J. Wu, Y. Li, J. Kubota, K. Domen, M. Aagesen, T. Ward, A. Sanchez, R. Beanland, Y. Zhang, M. Tang, S. Hatch, A. Seeds, H. Liu, *Nano Lett.* 14 (2014) 2013–2018.
- [6] S. Hu, C.Y. Chi, K.T. Fountaine, M. Yao, H.A. Atwater, P.D. Dapkus, N.S. Lewis, C. Zhou, *Energy Environ. Sci.* 6 (2013) 1879–1890.
- [7] T. Niidome, M. Fujii, N. Nakashima, Y. Katayama, Y. Niidome, Imaging mass spectrometry of gold nanorods distributed in tumor tissues, *Chem. Lett.* 44 (2015) 931–933.
- [8] S. Wang, Y. Hou, S. Lin, X. Wang, Water oxidation electrocatalysis by a zeolitic imidazolate framework, *Nanoscale* 6 (2014) 9930–9934.
- [9] C. Zheng, Z. Zhu, S. Wang, Y. Hou, NaF-assisted hydrothermal synthesis of Ti-doped hematite nanocubes with enhanced photoelectrochemical activity for water splitting, *Appl. Surf. Sci.* 359 (2015) 805–811.
- [10] Y. Hou, C. Zheng, Z. Zhu, X. Wang, Microwave-assisted fabrication of porous hematite photoanodes for efficient solar water splitting, *Chem. Comm.* 52 (2016) 6888–6891.
- [11] A. Paracchino, V. Laporte, K. Sivula, M. Grätzel, E. Thimsen, *Nat. Mater.* 10 (2011) 456–461.
- [12] J. Wang, P. Zhang, X. Song, L. Gao, *RSC Adv.* 4 (2014) 27805–27810.
- [13] M.H. Lee, K. Takei, J. Zhang, R. Kapadia, M. Zheng, Y.Z. Chen, J. Nah, T.S. Matthews, Y.L. Chueh, J.W. Ager, A. Javey, *Angew. Chem. Int. Ed.* 51 (2012) 10760–10764.
- [14] M.J. Kenney, M. Gong, Y. Li, J.Z. Wu, J. Feng, M. Lanza, H. Dai, *Science* 342 (2013) 836–840.
- [15] X. Qi, G. She, X. Huang, T. Zhang, H. Wang, L. Mu, W. Shi, *Nanoscale* 6 (2014) 3182–3189.
- [16] Y.J. Hwang, C.H. Wu, C. Hahn, H.E. Jeong, P. Yang, *Nano Lett.* 12 (2012) 1678–1682.
- [17] Y. Hou, B.L. Abrams, P.C.K. Vesborg, M.E. Bjorketun, K. Herbst, L. Bech, A.M. Setti, C.D. Damsgaard, T. Pedersen, O. Hansen, J. Rossmeisl, S. Dahl, J.K. Norskov, I. Chorkendorff, *Nat. Mater.* 10 (2011) 434–438.
- [18] S.W. Boettcher, E.L. Warren, M.C. Putnam, E.A. Santori, D. Turner-Evans, M.D. Kelzenberg, M.G. Walter, J.R. McKone, B.S. Brunschwig, H.A. Atwater, N.S. Lewis, *J. Am. Chem. Soc.* 133 (2011) 1216–1219.
- [19] E.L. Warren, J.R. McKone, H.A. Atwater, H.B. Gray, N.S. Lewis, *Energy Environ. Sci.* 5 (2012) 9653–9661.
- [20] I. Oh, J. Kye, S. Hwang, *Nano Lett.* 12 (2012) 298–302.
- [21] K. Jun, Y.S. Lee, T. Buonassisi, J.M. Jacobson, *Angew. Chem. Int. Ed.* 124 (2012) 438–442.
- [22] K. Sun, X. Pang, S. Shen, X. Qian, J.S. Cheung, D. Wang, *Nano Lett.* 13 (2013) 2064–2072.
- [23] K. Sun, N. Park, Z. Sun, J. Zhou, J. Wang, X. Pang, S. Shen, S.Y. Noh, Y. Jing, S. Jin, P.K.L. Yu, D. Wang, *Energy Environ. Sci.* 5 (2012) 7872–7877.
- [24] Y. Ling, G. Wang, D.A. Wheeler, J.Z. Zhang, Y. Li, *Nano Lett.* 11 (2011) 2119–2125.
- [25] X. Lian, X. Yang, S. Liu, Y. Xu, C. Jiang, J. Chen, R. Wang, *Appl. Surf. Sci.* 258 (2012) 2307–2311.
- [26] A. Memar, C.M. Phan, M.O. Tade, *Int. J. Hydrogen Energy* 37 (2012) 16835–16843.
- [27] P.S. Shinde, G.H. Go, W.J. Lee, *J. Mater. Chem.* 22 (2012) 10469–10471.
- [28] W.J. Lee, P.S. Shinde, G.H. Go, C.H. Doh, *Int. J. Hydrogen Energy* 39 (2014) 5575–5579.
- [29] S.K. Mohapatra, S.E. John, S. Banerjee, M. Misra, *Chem. Mater.* 21 (2009) 3048–3055.
- [30] A. Duret, M. Gratzel, *J. Phys. Chem. B* 109 (2005) 17184–17191.
- [31] A.B.F. Martinson, M.J. DeVries, J.A. Libera, S.T. Christensen, J.T. Hupp, M.J. Pellin, J.W. Elam, *J. Phys. Chem. C* 115 (2011) 4333–4339.
- [32] A. Fujimori, M. Saeki, N. Kimizuka, M. Taniguchi, S. Suga, *Phys. Rev. B* 34 (1986) 7318–7328.
- [33] F.J. Morin, *Phys. Rev.* 83 (1951) 1005–1010.
- [34] S. Li, P. Zhang, X. Song, L. Gao, *ACS Appl. Mater. Inter.* 7 (2015) 18560–18565.
- [35] Z. Zhang, M.F. Hossain, T. Takahashi, *Appl. Catal. B: Environ.* 95 (2010) 423–429.
- [36] A. Kargar, S.J. Kim, P. Allameh, C. Choi, N. Park, H. Jeong, Y. Pak, G.Y. Jung, X. Pan, D. Wang, S. Jin, *Adv. Funct. Mater.* 25 (2015) 2609–2615.
- [37] P. Zhang, L. Gao, X. Song, J. Sun, *Adv. Mater.* 27 (2015) 562–568.